The International Journal of Advanced Manufacturing Technology (2026) 143:819–840
https://doi.org/10.1007/s00170-026-17545-4

ORIGINAL ARTICLE

Physics-Based porosity prediction in powder bed fusion – laser beam using a thermal simulation algorithm

Ibrahim Ulke[1] · **Oguzhan Yilmaz**[1] · **Mehmet Mollamahmutoglu**[2]

Received: 25 September 2025 / Accepted: 16 January 2026 / Published online: 10 February 2026
© The Author(s) 2026

Abstract
Powder Bed Fusion–Laser Beam (PBF-LB) is a widely used additive manufacturing technique that enables the fabrication of geometrically complex components, yet it remains susceptible to internal defects, particularly porosity, which can compromise mechanical performance. This study presents a physics-based thermal simulation algorithm developed to predict porosity in Ti6Al4V parts fabricated via PBF-LB without relying on extensive training datasets. The algorithm numerically solves the transient three-dimensional heat conduction problem using the finite volume method, incorporating temperature-dependent material properties, a Gaussian-distributed laser heat source, and relevant thermal loss mechanisms. To validate the predictive capability of the model, six Ti6Al4V specimens were fabricated under varying process parameters using a PBF-LB system, and porosity levels were experimentally evaluated through Archimedes density measurements and high-resolution X-ray micro-Computed Tomography (μ-CT). Additional characterization by Scanning Electron Microscopy (SEM), optical microscopy, and Energy-Dispersive X-ray Spectroscopy (EDS) was performed on cross-sectioned subsurface regions to assess pore morphology and elemental homogeneity. The porosity values predicted by the simulation algorithm exhibited strong agreement with experimental findings in terms of trend and ranking, with predicted porosity ranging from 4.78% to 15.75% and μ-CT results ranging from 3.54% to 13.41%, thereby demonstrating the model's effectiveness in capturing the relative impact of process parameters on porosity formation in PBF-LB fabricated components.

Keywords Porosity prediction · Thermal modeling · Ti6Al4V alloy · Additive manufacturing

1 Introduction

Additive Manufacturing (AM) is a technique that enables the production of complex parts that are difficult or impossible to fabricate using conventional methods by building them layer by layer [1]. It also offers greater design flexibility, minimizes raw material consumption, and eliminates the need for additional tooling compared to traditional manufacturing approaches [2]. Owing to these advantages, it has found widespread application in aerospace, automotive, biomedical, and energy sectors. However, defects such as porosity, cracking, and anisotropic material properties inherent to layer-based fabrication can significantly impair the mechanical performance and reliability of the final parts [3]. Because of their high strength-to-weight ratio, resistance to corrosion, and biocompatibility, alloys like Ti6Al4V are used extensively in the aerospace and biomedical industries, making internal structure prediction crucial in additive manufacturing.

Powder Bed Fusion–Laser Beam PBF-LB is one of the most widely used powder bed fusion technologies. This method allows the selective melting of metal powder with a high-energy laser beam, layer by layer, and the production of complex geometry parts with high precision in a directly usable form. However, accurate calibration and optimization of process parameters such as laser power, scanning speed, layer thickness, and powder density are essential to ensure part quality and process stability. Any error or mismatch in these parameters directly affects the energy density transferred to the material [4]. As a result of the changing Volumetric Energy Density (VED), defects can occur in the

✉ Ibrahim Ulke
ibrahimulke@gazi.edu.tr

[1] Department of Mechanical Engineering, Faculty of Engineering, Gazi University, Ankara 06570, Turkey

[2] Department of Aerospace Engineering, Faculty of Aeronautics and Astronautics, Ankara Yıldırım Beyazıt University, Ankara 06010, Türkiye

produced part, which directly affect the final product quality. While VED provides a simplified framework to describe the amount of energy delivered to the material, recent studies have shown that it does not fully capture the complexity of melt pool dynamics or defect formation mechanisms [5, 6]. In particular, VED fails to account for temporal laser-material interaction effects, scan path strategies, and thermal accumulation across layers [7]. Although VED is used in this study to provide a baseline comparison among process conditions, its predictive capability is limited. Therefore, it is complemented by a physics-based thermal simulation that models transient heat flow and temperature-dependent material behavior at the voxel level for a more accurate prediction of porosity formation.

Lack of fusion, keyhole instability, and gas porosity are recognized as the primary mechanisms of pore formation in PBF-LB processes [8, 9]. Under high energy densities, keyhole-induced voids may form as a result of an unstable vapor depression that collapses and traps vapor pockets inside the solidifying melt pool contrary to earlier assumptions. This phenomenon is not caused directly by evaporation but by the dynamic instability of the vapor cavity itself [10]. Lack of fusion, on the other hand, occurs due to insufficient overlap between adjacent melt pools or successive layers, often due to suboptimal combinations of laser power, scan speed, hatch spacing, or layer thickness [11]. Although lack of fusion may manifest as internal pores within the part, it is characterized by irregularly shaped, elongated voids typically located along layer boundaries or scan track interfaces, reflecting inadequate melting or bonding rather than trapped gas [12]. Both defect types directly compromise the density, strength, and fatigue resistance of the final component [13]. Therefore, eliminating such defects prior to production through predictive modeling is critical to improving the quality and reliability of parts manufactured using PBF-LB. To promote wider industrial adoption of PBF-LB technology, time and cost-efficient process optimization strategies must be developed to prevent internal defects before fabrication begins. The literature presents various approaches for defect detection and mitigation. Among these, Non-Destructive Testing (NDT) methods such as X-ray micro-Computed Tomography (μ-CT) and ultrasonic inspection are widely used for post-process defect detection, whereas defect prevention relies on process parameter optimization, in-situ monitoring, and predictive modeling techniques [14, 15].

Machine Learning (ML) has emerged as a powerful tool for predicting defect formation and optimizing process parameters in layered manufacturing processes. Models such as Support Vector Machines (SVM) and decision trees have been applied to porosity prediction using various feature sets derived from process parameters [16–18]. For instance, Pi et al. developed four different porosity prediction models by applying the DBSCAN algorithm on Archimedes density measurements of 49 Inconel 718 specimens fabricated with PBF-LB [19]. However, their findings indicate that even after outlier removal and data cleaning, the models exhibited considerable variability in prediction accuracy. Similarly, Faizan Mohamed et al. proposed a reinforcement learning approach supported by the Eagar-Tsai thermal model, trained on laser power, scan speed, and inter-scan distance as inputs [20]. They experimentally validated their results using 12 different process parameter combinations with A205 aluminum alloy powder. Despite incorporating a physics-based model, their study also required extensive data cleaning and exhibited inconsistencies between predicted and actual porosity values. In another study, Staszewska et al. combined machine learning classification techniques with regression analysis to identify porosity types in PBF-LB-fabricated AlSi10Mg specimens [16]. As with most ML-based frameworks, their pipeline involved manual labeling, geometric feature extraction, data filtering, and training, which are time-consuming and labor-intensive. A review of the existing literature reveals that ML models for porosity prediction typically require large volumes of high-quality, labeled data to perform effectively [21]. Despite their potential, these models are typically not generalizable. They tend to match closely to certain datasets or process windows, which makes them less useful in other situations [22, 23]. Furthermore, in real-time quality control applications, the primary source of latency is not the inference speed of the trained model. Instead, the delays arise from data acquisition, preprocessing, and integration with machine control algorithms [24, 25]. These system-level bottlenecks can impair timely decision-making and compromise the responsiveness of feedback control systems in PBF-LB. To promote wider adoption of PBF-LB technology, both detection and prevention strategies must be employed to reduce internal structural defects before and during production. These strategies can be broadly categorized into three groups: non-destructive methods, destructive analysis, and in-situ process monitoring. Non-destructive techniques such as μ-CT [26, 27], ultrasonic inspection [28, 29], and infrared thermography [30] are widely used to detect internal porosity post-fabrication. Destructive methods, including cross-sectional microscopy and density measurements via the Archimedes principle, are commonly used for validation and calibration purposes [31]. In contrast, in-situ monitoring approaches focus on detecting and correcting defects in real time during the build process, using optical sensors, pyrometers, or thermal cameras integrated into the machine [32].

In recent years, ML has been applied across all three categories, particularly in in-situ monitoring and defect classification tasks. However, ML itself is not a standalone category,

but rather a computational tool used to enhance decision-making based on sensor data or experimental results [33]. Models such as Support Vector Machines (SVM) and decision trees have been proposed to predict porosity and optimize process parameters based on labeled datasets [34]. For instance, Pi et al. and Faizan Mohamed et al. utilized SVM and reinforcement learning, respectively, to identify defect-prone parameter regions. Yet, recent work has shown that lack of fusion regions in process maps do not follow hard classification boundaries but rather exhibit gradual transitions depending on thermal history and melt pool morphology [35]. This suggests that traditional classification models may have limited accuracy in capturing such complex and continuous boundaries without additional physical context or hybrid modeling approaches. Therefore, ML models must be carefully validated and possibly combined with physics-based models to improve robustness and generalizability in porosity prediction tasks [36, 37]. When the literature is examined, the size and change of the melt pool can be predicted before production starts, as an approach different from machine learning with the use of artificial intelligence. It is clearly seen that internal structure analysis can be performed based on process parameters in various melt pool models developed for this purpose. In the PBF-LB method, modeling the melt pool dynamics correctly and optimizing the process parameters requires computer-based simulation approaches as an alternative to the experimental trial-and-error method [38]. In this context, numerical models including physical processes such as thermal conduction, mass transfer, and laser absorption are widely used to predict melt pool dimensions and surface morphology. Numerical models based on the direct finite element method, such as in the study by Slama et al., are also widely available in the literature aiming at porosity prediction [39]. In particular, models developed based on volumetric heat sources provide a critical tool in understanding the effects of parameters such as laser power, scanning speed, and powder layer properties on energy distribution within the material. However, such models included partial error rates in the past because they considered parameters such as laser absorptivity and heat conduction coefficient that change with temperature as fixed values. As a result of studies conducted in recent years, the changes of these material-dependent properties with temperature have been better understood and explained. Thanks to these developments, the compatibility with experimental results in melt pool modeling has increased and porosity estimation from melt pool geometry has become more possible. Adapting the temperature-dependent changes of parameters such as the heat conduction coefficient or laser absorptivity, which directly affect the melt pool geometry, to mathematical models is challenging. This process also leads to an increase in processing load and calculation times. To reduce the calculation time, simulation models that include certain approaches and assumptions to estimate melt pool dimensions are available in the literature [40].

Although various CFD-based models have been proposed in the literature to simulate melt pool dynamics, often calibrated using single-track laser scan experiments [41], these models generally suffer from high computational cost and limited scalability. Most focus on microscale or short-time simulations and are not feasible for full-layer or volumetric porosity prediction in practical build domains. Furthermore, many rely on constant thermophysical properties and neglect inter-layer thermal interactions and cumulative heat effects, which are essential for capturing defect formation mechanisms in multi-layer PBF-LB processes. To address these limitations, the present study proposes a voxel-based, finite volume simulation framework that models transient heat conduction across a three-dimensional build domain using temperature-dependent material properties. The build space is discretized into thermal voxels, and the heat equation is solved layer by layer using OpenMP-based parallelization to ensure computational efficiency. The algorithm predicts porosity by directly analyzing key process parameters such as laser power, scanning speed, layer thickness, and initial temperatures without requiring large datasets or extensive training, as required in ML approaches. Its flexible structure allows adaptation to different materials and process settings. Experimental validation was performed using Ti6Al4V specimens produced under multiple parameter combinations, with porosity quantified via Archimedes density measurements. The results demonstrate that the proposed method offers a fast, scalable, and physically grounded tool for porosity prediction and process optimization in PBF-LB, contributing to enhanced quality control and broader industrial applicability of the technology.

2 Materials and methods

A schematic representation of the PBF-LB process is provided in Fig. 1. The illustration emphasizes the principal components of the system, including the laser source, galvanometer-driven beam steering unit, and powder bed, along with the underlying physical phenomena such as steep thermal gradients, vaporization, and lack-of-fusion defects. This schematic serves as a conceptual framework for understanding the role of localized heat input in governing melting and solidification within the powder bed, which in turn dictates defect formation mechanisms. To facilitate a clearer understanding of the study, the subsequent sections are organized under specific subheadings, wherein the materials, experimental setup, process parameters, and numerical framework are presented in detail.

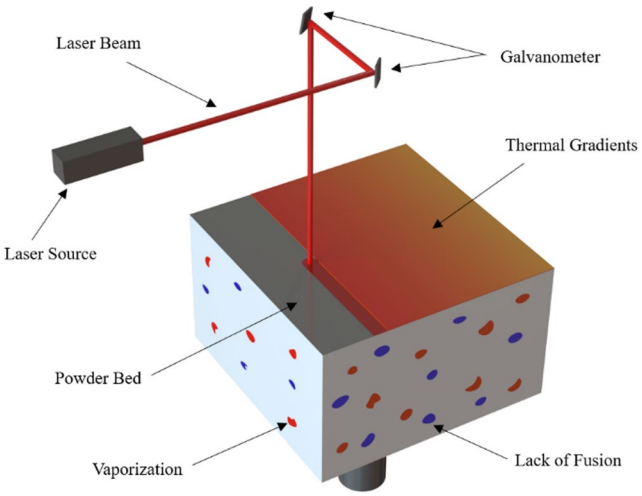


Fig. 1 Schematic of laser scanning and thermal gradients in PBF-LB

2.1 Fabrication and characterization of Ti6Al4V specimens

This study presents a hybrid methodology that integrates experimental characterization with a physics-based thermal simulation model to accurately capture the mechanisms governing porosity formation in laser-based additive manufacturing. Within this framework, six Ti6Al4V specimens were produced on a Sisma MYSINT100 PBF-LB system under distinct combinations of laser power, scanning speed, and scanning strategy. To further assess the predictive capability of the proposed algorithm, an additional set of Ti6Al4V specimens with dimensions of 10 mm × 10 mm × 5 mm was fabricated using gas-atomized powder on a PBF-LB system equipped with a 200 W Yb-fiber laser operating at a wavelength of 1070 nm (Fig. 2) [42]. Throughout the build process, environmental conditions were tightly controlled, with humidity maintained at 0–20 ppm, chamber pressure at 7–12 mbar, oxygen concentration at 0–100 ppm, and argon shielding gas provided at a flow rate of 35 L/min.

Table 2 Individual process parameter sets used for the fabrication of the three specimens

Process Parameters	Laser Power (W)	Scan Speed (mm/s)	Scan Strategy	VED (J/mm^3)
Sample 1	100	300	Stripe	167
Sample 2	140	350	Stripe	175
Sample 3	180	400	Stripe	200
Sample 4	100	300	Zigzag	167
Sample 5	140	350	Zigzag	175
Sample 6	180	400	Zigzag	200

A 45° rotation angle was applied between adjacent layers to promote uniform energy distribution across the build. The fixed process parameters adopted in the simulations are summarized in Table 1. Each specimen was fabricated under a distinct set of conditions, involving different combinations of laser power, scan speed, and scan strategy, as presented in Table 2. The experimental validation performed in this study is limited to two commonly used scan strategies (zigzag and stripe), and therefore the robustness of the model should be interpreted within this restricted scan-strategy domain.

The microstructural characteristics and chemical homogeneity of the fabricated Ti6Al4V specimens were analyzed using Scanning Electron Microscopy (SEM) in conjunction

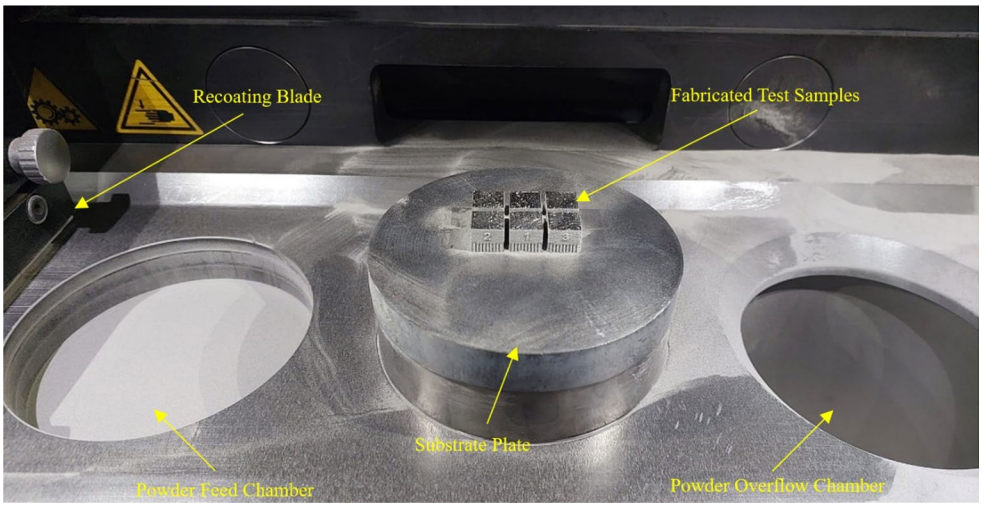


Fig. 2 Sample fabrication in SismaMYSINT100

Table 1 General PBF-LB process parameters used for all specimens

ProcessParameters	ParticleSize	Laser Spot Size	Substrate Temperature	Hatch Spacing	Layer Thickness
Sample 1–6	(D10–D90): 15–45 µm	55 µm	0–50 °C	50 µm	40 µm

with Energy Dispersive X-ray Spectroscopy (EDS). SEM imaging was utilized to examine the surface morphology, melt pool features, and porosity-related defects at high magnifications. EDS analysis was performed using a Zeiss SmartEDX system under an accelerating voltage of 20 kV, a magnification of 1000×, and a live acquisition time of 60 s. All spectra were collected using Full Area EDS mapping, rather than point analysis, to provide a representative assessment of the elemental distribution.

Following fabrication, each specimen was examined using high-resolution µ-CT with a ZEISS Xradia 510 Versa system to non-destructively quantify internal porosity. The µ-CT analysis provided comprehensive insights into total porosity, pore morphology, volumetric distribution, and spatial characteristics. The acquired image stacks in DICOM (.dcm) format were subsequently imported into Dragonfly software (ORS Comet Technologies, Canada) for three-dimensional visualization and segmentation of pore structures.

2.2 Process workflow: from production to porosity prediction via thermal modeling

An integrated methodology was employed to capture porosity formation mechanisms in laser-based additive manufacturing by synchronizing experimental characterization with numerical thermal modeling. As illustrated in Fig. 3, the workflow comprises two complementary and converging pathways: experimental validation and computational prediction. Ti6Al4V specimens were fabricated using two distinct scanning strategies (zigzag and stripe) and subsequently analyzed by high-resolution µ-CT, SEM, EDS, and optical microscopy. Together, these techniques yielded comprehensive insights into internal porosity, surface morphology, and chemical homogeneity. In parallel, fabrication parameters were incorporated into a finite volume-based thermal simulation framework developed to predict porosity through spatial and temporal heat conduction analysis. The consistent alignment of parameters across experimental and numerical domains enabled direct comparison between predicted and observed porosity, thereby reinforcing the robustness and reliability of the proposed algorithm.

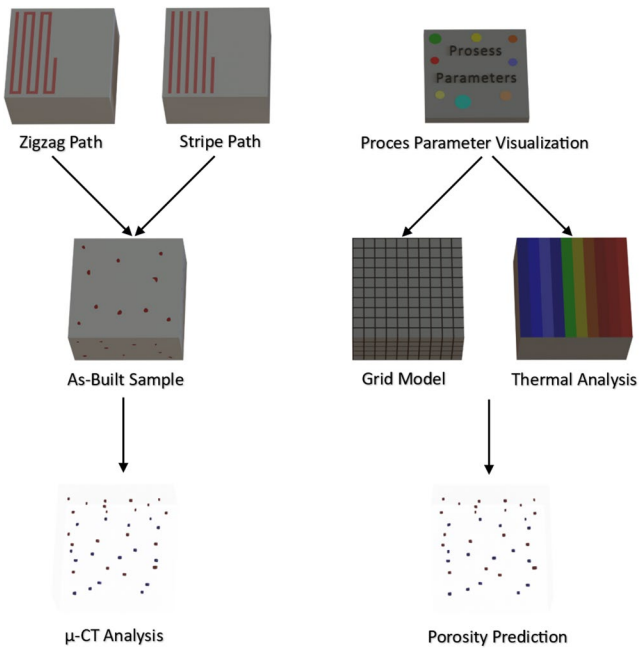


Fig. 3 Schematic representation of process workflow: from PBF-LB path strategy to porosity prediction and experimental validation

2.3 Mathematical background of the algorithm

Energy input per unit volume, commonly expressed as VED, has traditionally been used as a combined metric to correlate process parameters such as laser power, scan speed, hatch spacing, and layer thickness [43–45]. While extensively adopted in the literature, this scalar measure oversimplifies the intrinsically transient and three-dimensional characteristics of the PBF-LB process. To address these shortcomings, the developed simulation algorithm numerically resolves the transient three-dimensional heat conduction problem through the finite volume method. The model further incorporates temperature-dependent material properties, phase transitions, laser–material interactions, and the sequential deposition of powder layers.

The developed simulation algorithm resolves the transient three-dimensional heat conduction problem in PBF-LB using the finite volume method. The framework incorporates temperature-dependent material properties, phase transitions, laser–material interactions, and the sequential addition of powder layers. For Ti6Al4V, temperature-dependent properties are represented through empirical piecewise linear functions. As an example, the specific heat capacity $c_p\,(T)$ is defined as Eq. 1 [46].

Absorptivity, which defines the fraction of incident laser energy absorbed by the material, is a key parameter in heat source modeling. In the algorithm, absorptivity is defined for different material states as follows: powder absorptivity (α_p) is 0.74, while solid (α_s) and liquid (α_l) absorptivity are set to 0.55 [47]. These values reflect the higher energy absorption capacity of powder due to its increased surface area and scattering characteristics. The effective absorptivity is dynamically calculated at each voxel depending on its position within the powder bed, phase state, and local occupancy conditions. For surface regions or partially melted layers, the model applies weighting schemes to simulate reduced absorption with depth or increased absorption in loosely packed regions.

To incorporate the effect of thermal resistance arising from porosity, a polynomial multiplier µ(θ) was introduced

into the effective thermal conductivity formulation. This multiplier penalizes heat conduction in underfilled regions as a function of the local occupancy ratio (θ), with its complete expression, empirically derived through curve fitting, presented in Table 3 (Eq. 6). In the model implementation, μ(θ) is squared to further suppress conductivity in regions of pronounced porosity, particularly in lack-of-fusion zones where loosely packed powder acts as a thermal insulator. By contrast, gas-induced keyhole pores generally contain no residual powder and therefore impose comparatively lower thermal resistance. In regions of full melting (fl.max = 1), the model reverts to solid-phase conduction or applies the packing-dependent formulation when the voxel lies at the powder–substrate interface.

Laser–material interaction was represented by a volumetric heat source with a Gaussian distribution, capturing the spatial energy profile of the continuous-wave laser beam. The absorbed laser energy is spatially distributed across the surface layer using analytical integration of a two-dimensional Gaussian profile via error functions. The corresponding surface-layer heat input function $Q_{source}(x, y)$ is presented in Table 3 (Eq. 7) where (x_0, y_0) denotes the instantaneous center of the laser beam on the substrate, and R is the beam radius. This formulation ensures the heat input is smoothly distributed across multiple voxels, preventing numerical instabilities.

In the simulation, heat dissipation from the part surface to the surrounding environment is modeled through two simultaneous mechanisms: natural convection and thermal radiation. These losses are computed for each surface voxel using the heat loss function, and the resulting values are added to the total energy balance as a sink term Q_{sink}. Total heat loss across a voxel face is calculated using the expression shown in Table 3 (Eq. 8), which accounts for the ambient gas temperature, material emissivity, and convective heat transfer coefficient.

Physically, this heat-loss term represents the removal of thermal energy from surfaces that are directly exposed to the chamber environment, thereby preventing unrealistic temperature accumulation at the boundaries. Natural convection captures the transfer of heat into the surrounding inert gas through gas–solid interaction, while thermal radiation accounts for the radiative emission of energy from hot surfaces to the cooler chamber walls. Together, these mechanisms emulate the primary pathways through which a real PBF-LB melt pool and its surrounding powder dissipate heat during processing, ensuring that the simulated temperature field reflects the thermal interactions occurring within the build chamber.

In the implementation of this term, the surrounding temperature (T_{surr}) was assigned a constant value of 300 K, corresponding to the measured chamber temperature during fabrication. This steady value reflects the thermally stable environment maintained inside the sealed build enclosure. For each voxel face identified as exposed, the heat-loss contribution computed from Eq. (8) is incorporated directly into the local energy balance as a negative source term, allowing surface cooling effects to be represented in a geometry-dependent manner without introducing additional temporal variations unrelated to the laser–material interaction.

The numerical framework employed in this study exclusively solves the transient heat conduction equation using a Finite Volume Method (FVM), without coupling fluid flow or solving the Navier–Stokes equations. As a result, melt pool dynamics such as convection or recoil pressure are not explicitly captured. Instead, the liquid fraction at each voxel is determined through a temperature-based empirical relation. This relation estimates the melt state through linear interpolation between the material's solidus (T_s) and liquidus (T_l) temperatures, as defined in Table 3 (Eq. 9).

For Ti6Al4V, the solidus (T_s) and liquidus (T_l) temperatures are taken as 1877 K and 1923 K, respectively [48]. This function is implemented in the C-based simulation code as the liquid ratio routine, which is invoked voxel-wise at each time step via the liquid array function. Within this framework, Occ(n) denotes the occupancy ratio of the n-th voxel layer, defined as the fraction of the cell volume occupied by consolidated material (ranging from 0 for fully void to 1 for fully dense). These temperature-driven formulations efficiently capture the phase transitions required for porosity estimation and latent heat accommodation, while enabling large-scale, layer-wise simulations without the computational overhead of fluid dynamics solvers.

Heat conduction into the build plate is implicitly modeled through the finite volume discretization of the heat equation, where inter-voxel heat transfer is computed in all six Cartesian directions (Fig. 4). Thermal conduction from the powder bed into the substrate is represented by the vertical heat flux in the –z direction ("up" flux) between adjacent thermal voxels. At the bottom boundary ($z = 0$), where the powder bed interfaces with the build plate, temperature gradients are resolved based on local thermal conductivities and temperature differences, allowing heat to dissipate into the substrate. In this formulation, the substrate is treated as a semi-infinite solid, eliminating the need for an explicit thermal domain.

Convective and radiative heat losses are applied only to external, exposed surfaces via the heat loss function. At the build plate interface, these losses are neglected under the assumption of full thermal contact between the part and the substrate.

The identification of voxels exposed to the environment, and therefore subject to heat loss, is achieved by performing neighbor checks in all six Cartesian directions (±x, ±y, ±z).

Table 3 Thermophysical models and governing equations employed in the porosity prediction algorithm

Eq. No	Physical Phenomenon	Governing Equation/Expression
1	Specific heat capacity – Ti6Al4V	$c_p(T) = \begin{cases} 483 + 0.25T, & T < 500K \\ 483 + 0.25T + 62.5, & 500K \leq T \leq 1268 \\ 530 + 0.14T, & 1268K < T < 1877K \\ 530 + 0.14T + 6304, & 1877K \leq T \leq 1923K \\ 930, & T > 1923K \end{cases}$
2	Laser absorptivity by phase	$\alpha_{eff} = \begin{cases} \alpha_p = 0.74 & \text{powder region} \\ \alpha_l = 0.27 & \text{liquid region} \\ \alpha_l + (\alpha_p - \alpha_l)\, tanh\,(22000 \times C) & \text{transition region} \end{cases}$
3	Thermal conductivity – solid phase	$k_s(T) = \begin{cases} 3.3 + 0.012T, & T \leq 1268K \\ 0.016T - 3, & 1268K < T \leq 1923K \\ 0.0175T - 4.5, & T > 1923K \end{cases}$
4	Thermal conductivity – powder phase	$k_p(T) = 0.000328T + 0.079$
5	Effective thermal conductivity	$k_{eff}(T) = \begin{cases} k_s(T).\theta, & if\ f_{l.max} = 1 \\ (1 - f_{l.max}).k_p(T) + f_{l.max}.\mu(\theta)^2.k_s(T), & otherwise \end{cases}$
6	Porosity penalty multiplier	$\mu(\theta) = -8.8(1-\theta)^5 + 22.2(1-\theta)^4 - 21.1(1-\theta)^3 + 9.3(1-\theta)^2 - 2.6(1-\theta) + 1$
7	Laser heat input (Gaussian distribution)	$Q_{source}(x,y) \propto \left[erf\left(\frac{\sqrt{2}(x \mp 0.5 - x_0)}{R}\right)\right].\left[erf\left(\frac{\sqrt{2}(y \mp 0.5 - y_0)}{R}\right)\right]$
8	Heat loss – convection and radiation	$Q_{sink} = h.A.(T_{surr} - T) + \epsilon.\sigma.A.(T_{surr}^4 - T^4)$
9	Liquid fraction – phase change	$f_{liq}(T) = \begin{cases} 0 & if\ T < T_s \\ 1 & if\ T > T_l \\ \frac{T - T_s}{T_l - T_s} & if\ T_s \leq T \leq T_l \end{cases}$
10	Cumulative packing density	$C = \sum_{n=0}^{k-1}(Grid\ size \times Occ(n))$

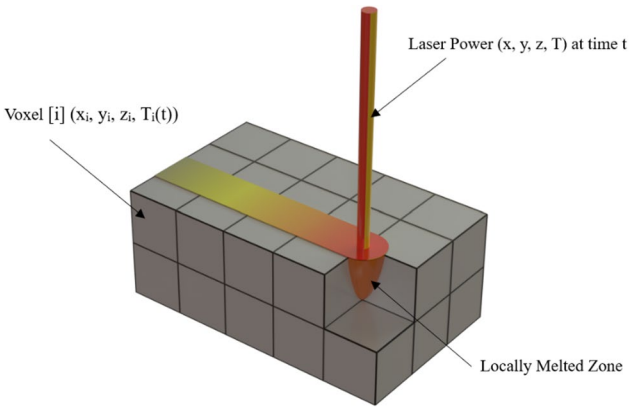


Fig. 4 A voxel-based thermal simulation representation of the laser–material interaction during PBF-LB. The laser is modeled as a moving heat source defined by its spatial coordinates (x, y, and z) and corresponding temperature T at time t. Each voxel is thermally evaluated with its own temperature field $T_i(t)$ over time

When a neighboring voxel is unoccupied, the corresponding face is designated as a boundary surface. This procedure enables localized and geometry-dependent heat dissipation, particularly at the top powder surfaces and lateral melt pool boundaries.

After the temperature field is updated, the algorithm evaluates the local liquid fraction and correspondingly adjusts the peak melt ratio. If sufficient melting is detected above a partially occupied voxel, the collapse function is invoked to simulate downward material redistribution, thereby capturing potential pore closure or densification effects. The time-step counter is then advanced, and the laser beam position is updated according to the selected scan strategy. Upon completion, the algorithm exports temperature, liquid fraction, and occupancy distributions for subsequent post-processing and visualization.

2.4 Numerical solver and porosity prediction framework

The numerical solver employed in this study was developed entirely in-house and implemented in C using an explicit Finite Volume Method (FVM) formulation. The computational domain was discretized into uniform cubic voxels, and the transient heat conduction equation was iteratively solved in three dimensions. Temperature updates for each control volume were obtained through an energy balance scheme that incorporated directional heat fluxes in the ±x, ±y, and ±z directions. At each iteration, thermal conductivity and specific heat capacity were dynamically updated as functions of temperature. Time integration was carried out using an explicit Euler scheme, with stability ensured by enforcing the Fourier number criterion. To accelerate layer-by-layer computations, the solver was parallelized with OpenMP, allowing voxel-level operations to be distributed across multiple CPU threads. Notably, no commercial or external multiphysics packages were utilized; the framework was developed entirely from the ground up as part of this research.

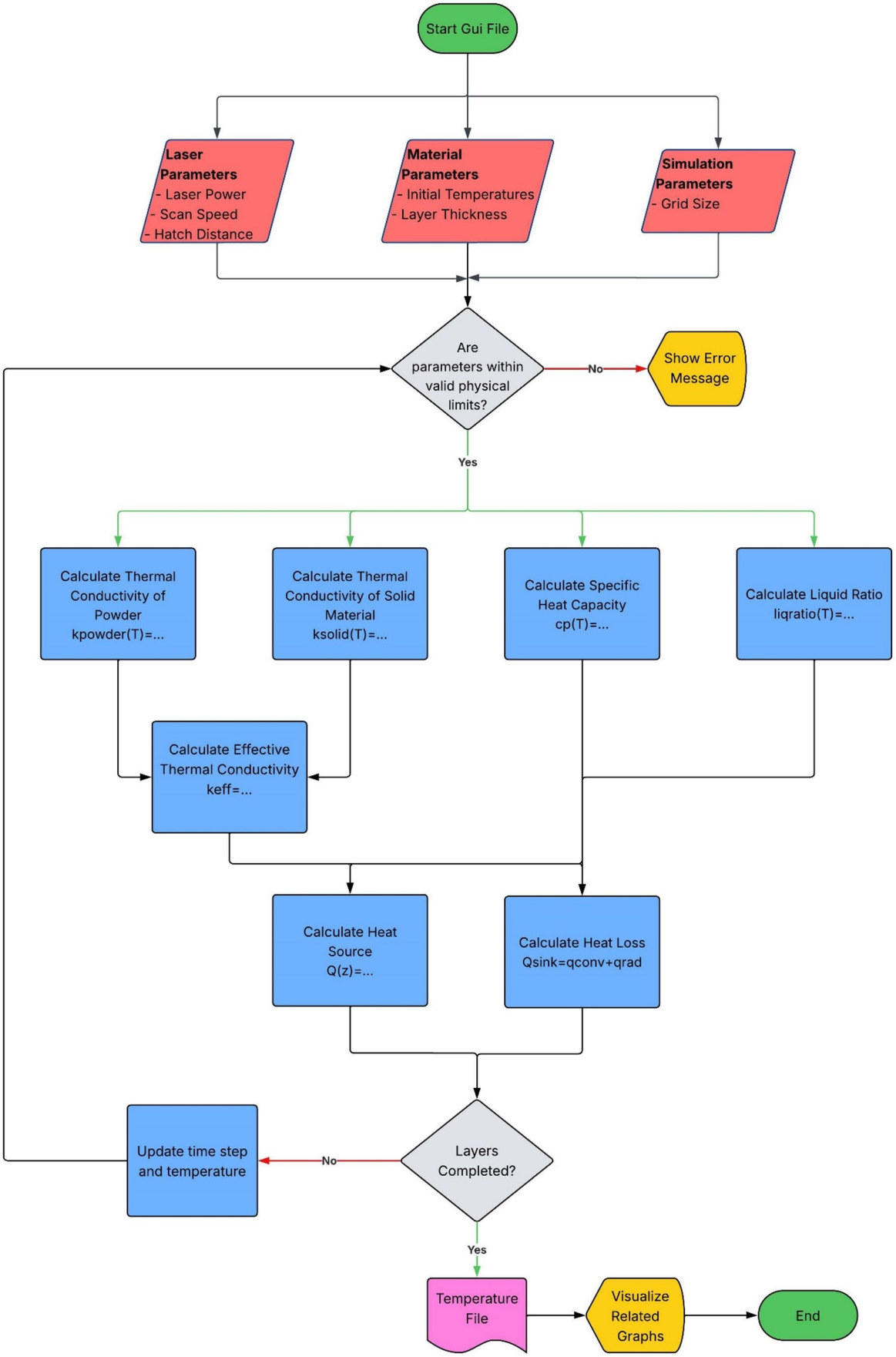
Fig. 5 Schematic workflow of the voxel-based thermal simulation algorithm for predicting porosity in PBF-LB processes

The present thermal framework is formulated strictly as a conduction-based model, without incorporating melt-pool fluid dynamics such as thermocapillary convection, recoil pressure, or free-surface motion. This modeling approach enables full-layer thermal simulations with high computational efficiency while capturing the dominant heat-transfer mechanisms associated with insufficient melting and thermally driven porosity formation. As illustrated in Fig. 5, the workflow begins with user-defined process parameters and domain initialization, followed by the layer-wise evaluation of transient temperature fields. At each time step, the model accounts for laser energy absorption, environmental heat losses (convection and radiation), and temperature-dependent material properties to represent the thermal behavior of the melt pool. Based on predefined temperature thresholds for Ti6Al4V, each voxel is classified according to its melting state, and the maximum liquid fraction reached during the build is recorded. Voxels that do not achieve complete melting or exhibit partial occupancy are flagged as underfilled, corresponding to potential porosity sites. Upon completion of the simulation, the volumetric porosity is quantified as the ratio of unfilled voxel volume to the total domain volume.

2.5 Thermal-to-porosity mapping strategy

Upon completion of the transient heat conduction simulation, porosity estimation was carried out based on the thermal history of individual voxels (Fig. 6). For each voxel, the maximum temperature attained during processing was recorded and compared against material-specific thresholds. Voxels that did not exceed the solidus temperature were classified as unmelted and assumed to remain in the powder state. Those with peak temperatures between the solidus and vaporization points were categorized as fully melted, whereas voxels surpassing the vaporization threshold were flagged as potential sites of keyhole-induced porosity.

To capture densification phenomena, a collapse routine was implemented in which molten material was redistributed into underlying partially filled voxels. Overall porosity was then quantified as the volume fraction of voxels with fill ratios remaining below unity after all melting and redistribution operations. This voxel-wise classification constitutes a physically consistent and computationally efficient approach for translating thermal histories into spatially resolved porosity distributions.


Start Gui File
Laser Parameters
- Laser Power
- Scan Speed
- Hatch Distance
Material Parameters
- Initial Temperatures
- Layer Thickness
Simulation Parameters
- Grid Size
Are parameters within valid physical limits?
No
Show Error Message
Yes
Calculate Thermal Conductivity of Powder kpowder(T)=...
Calculate Thermal Conductivity of Solid Material ksolid(T)=...
Calculate Specific Heat Capacity cp(T)=...
Calculate Liquid Ratio liqratio(T)=...
Calculate Effective Thermal Conductivity keff=...
Calculate Heat Source Q(z)=...
Calculate Heat Loss Qsink=qconv+qrad
Layers Completed?
No
Update time step and temperature
Yes
Temperature File
Visualize Related Graphs
End

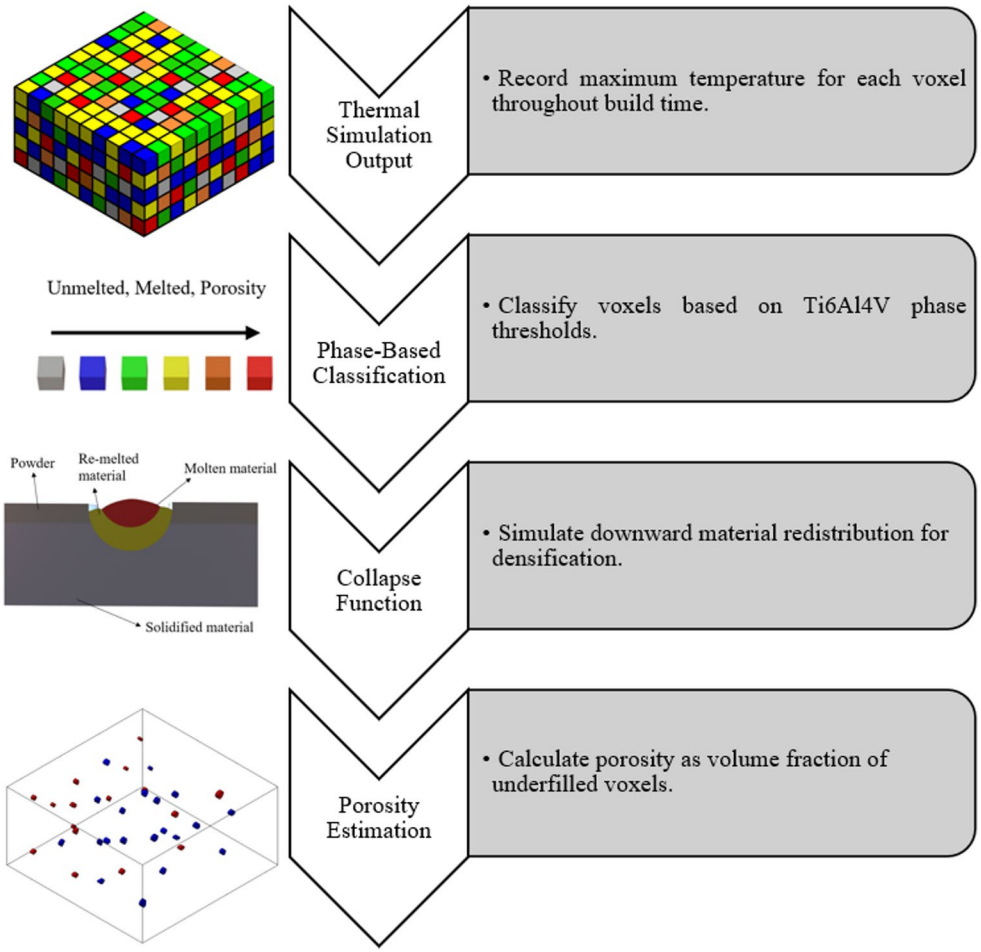


Fig. 6 Schematic representation of the thermal-to-porosity mapping strategy based on voxel-level simulation and phase-dependent material response

For visualization and interactive analysis, a custom graphical interface was developed in Python. The implementation combines Tkinter for the user interface, NumPy for numerical operations, and the napari viewer for voxel-wise rendering of porosity fields.

3 Results and discussion

3.1 Experimental validation of the developed algorithm and comparison with literature data on melt pool characteristics

The predictive capability of the developed algorithm for melt pool geometries was rigorously evaluated using cross-sectional measurements reported in the literature as benchmark references. Comparative analysis under three distinct processing conditions (Fig. 7) showed that the model successfully reproduced shallow, bowl-shaped melt pools at lower energy inputs, whereas its accuracy in predicting melt pool depth decreased under higher energy input conditions, where the geometries became significantly deeper and keyhole-like. These findings highlight both the sensitivity of the thermal simulation to process energy input and its relative limitation in capturing extreme melt pool depths.

It should also be noted that even in experimental studies reported in the literature, melt pool dimensions obtained under nominally identical process parameters often display noticeable variability, complicating direct one-to-one validation. Despite these challenges, the developed algorithm demonstrates superior predictive capability when compared with the analytical framework proposed by Dutta et al. [49] and the volumetric heat absorption-based numerical model of Mishra and Kumar [50].

3.2 Experimental measurement of porosity

After fabrication, the specimens were detached from the substrate using Electrical Discharge Machining (EDM) (Fig. 8). The relative densities of the specimens ($\rho_{measured}$) were then determined using the Archimedes density method, with the results summarized in Table 4.

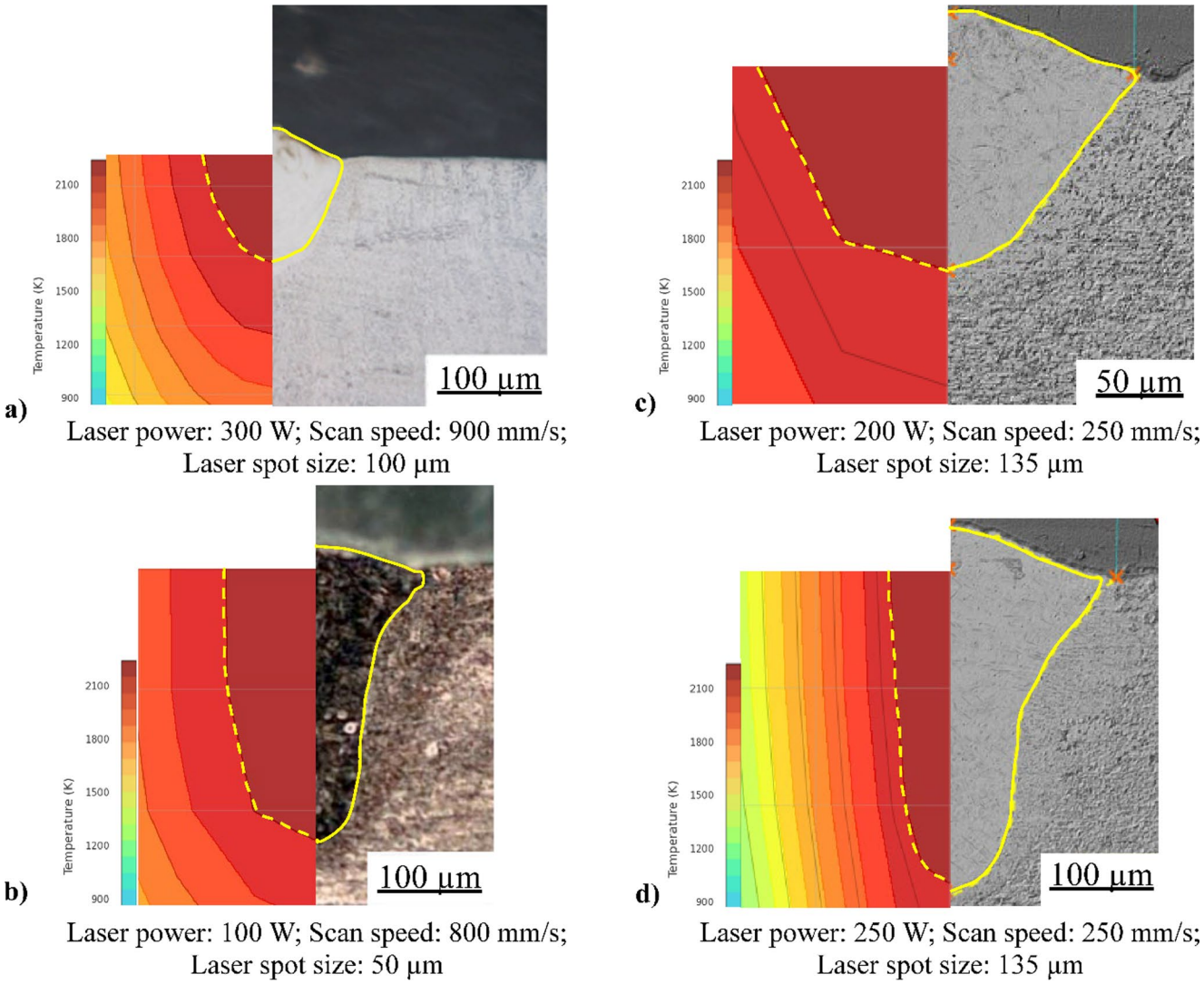


Fig. 7 Validation of predicted melt pool geometries against literature data for different process conditions: (**a**) [51]; (**b**) [52]; (**c**) [53]; (**d**) [53]

Measurements were performed at an ambient temperature of 25 °C, and relative density was calculated using Eqs. (11) and (12) [54]:

$$\rho_{measured} = \frac{m_{air} \times \left(\rho_{fluid} - \rho_{air}\right)}{m_{air} - m_{fluid}} + \rho_{air} \tag{11}$$

$$Porosity\ (\%) = 100 - \left(100 \times \frac{\rho_{measured}}{\rho_{Ti6Al4V}}\right) \tag{12}$$

where m_{air} represents the weight of the specimens in air; m_{fluid} represents the weight of the specimens in distilled water; ρ_{fluid} is the density of the distilled water at the measurement temperature (0.9973 gr/cm^3); ρ_{air} is the density of the air at the measurement temperature (0.0000011839 gr/cm^3); $\rho_{Ti6Al4V}$ is the theoretical density of Ti6Al4V (4.43 gr/cm^3).

As presented in Table 4, the porosity levels determined using the Archimedes method provide a quantitative basis for assessing the predictive accuracy of the developed model. Since the primary objective of this study is to validate the model's capability in predicting overall porosity ratios, the spatial characterization of pore distribution and morphology has been deferred to future investigations. Notably, the experimentally measured porosity trends exhibit strong correlation with variations in volumetric energy density, reaffirming its pivotal role in governing defect formation during laser-based additive manufacturing.

3.3 Surface morphology and pore distribution analysis via SEM and optical imaging

The surface quality and near-surface defect morphology of Ti6Al4V specimens fabricated via the PBF-LB process

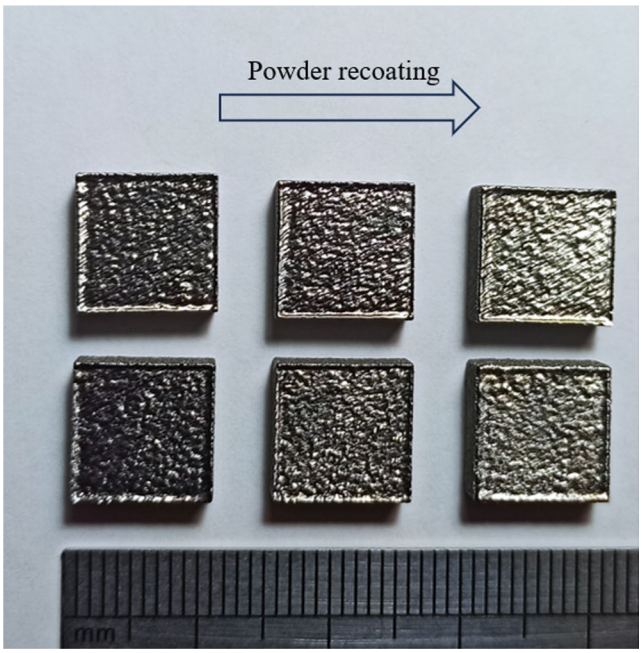


Fig. 8 Cubic specimens fabricated using a single set of process parameters for experimental validation

were characterized through microstructural analysis using both Scanning Electron Microscopy (SEM) and optical microscopy. These microscopy-based evaluations were not intended as independent methods of porosity quantification but were instead employed to provide qualitative validation of the spatial predictions generated by the thermal simulation algorithm. While the algorithm identifies defect-prone regions based on localized thermal gradients, melt pool stability, and energy input history, SEM and optical microscopy provided direct visual confirmation by revealing pore clustering, melt track irregularities, and morphological features indicative of keyhole- or lack-of-fusion–related defects.

Detailed SEM and optical microscopy analyses revealed pronounced variations in surface and near-surface porosity morphology among the Ti6Al4V specimens fabricated by the PBF-LB process (Figs. 9 and 10). In particular, specimens S3 and S6 exhibited a markedly higher pore density compared to the others. The observed pores were predominantly spherical or elliptical, occurring either as isolated voids or clustered formations, and were concentrated near the central melt regions of the build surface. Complementary optical microscopy confirmed these findings, revealing pronounced surface roughness and localized pore clustering along melt track boundaries in specimens S3 and S6. The spatial distribution of pores and irregular melt track morphology are consistent with keyhole-induced porosity, which typically arises under excessive energy input conditions.

3.4 Verification of chemical homogeneity using EDS

Verification of the thermal simulation algorithm developed for porosity prediction required ensuring that no significant elemental segregation or compositional deviations occurred during fabrication. Since the algorithm assumes consistent material properties derived from nominal Ti6Al4V data, any deviation in alloy composition could introduce discrepancies between predicted and actual thermal responses. To validate these thermophysical assumptions and exclude material variability as a confounding factor, EDS analysis was performed on all fabricated specimens. This characterization confirmed chemical homogeneity across the different process conditions, ensuring that the observed porosity trends could be attributed solely to variations in thermal history and energy input.

The EDS analysis confirmed that all six specimens exhibited an elemental composition consistent with nominal Ti6Al4V Grade 5 alloy (Fig. 11). Titanium was identified as the dominant element, ranging from 88.10% to 88.66% by weight, while aluminum and vanadium contents remained within the expected alloying limits, ranging from 6.37% to 6.62% and 4.98% to 5.49%, respectively. These minimal variations in elemental concentration indicate that no significant segregation or redistribution occurred during solidification, thereby validating the assumption of chemical homogeneity in the fabricated specimens.

3.5 Porosity evaluation via μ-CT analysis

The segmented porosity maps revealed heterogeneous spatial distributions, with variations in clustering, volume, and sphericity that were consistent with the applied process parameters (Fig. 12). Specimens S3 and S6, fabricated with the highest energy densities, exhibited the largest total pore volumes, whereas S1 and S4 displayed more uniform structures

Table 4 Density values obtained by the Archimedes method

Sample No	m_{air}(gr)	m_{fluid}(gr)	$\rho_{measured}$(gr/cm^3)	Porosity (%)
1	2.186	1.686	4.386	0.993
2	2.184	1.678	4.304	2.844
3	2.176	1.631	3.981	10.135
4	2.185	1.687	4.375	1.241
5	2.181	1.675	4.298	2.979
6	2.175	1.625	3.943	10.993

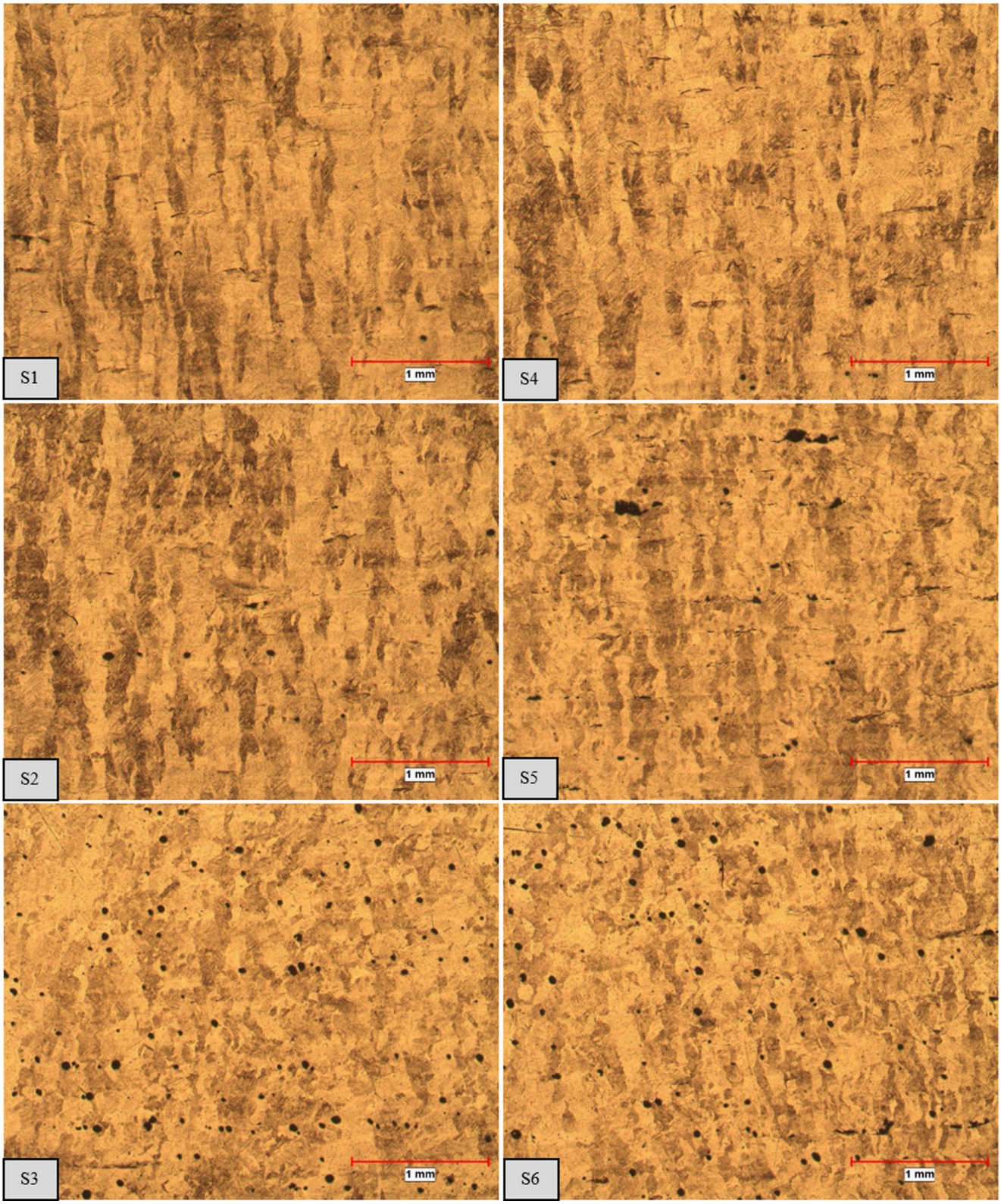


Fig. 9 Optical microscopy images showing the surface porosity and microstructure of specimens S1 to S6

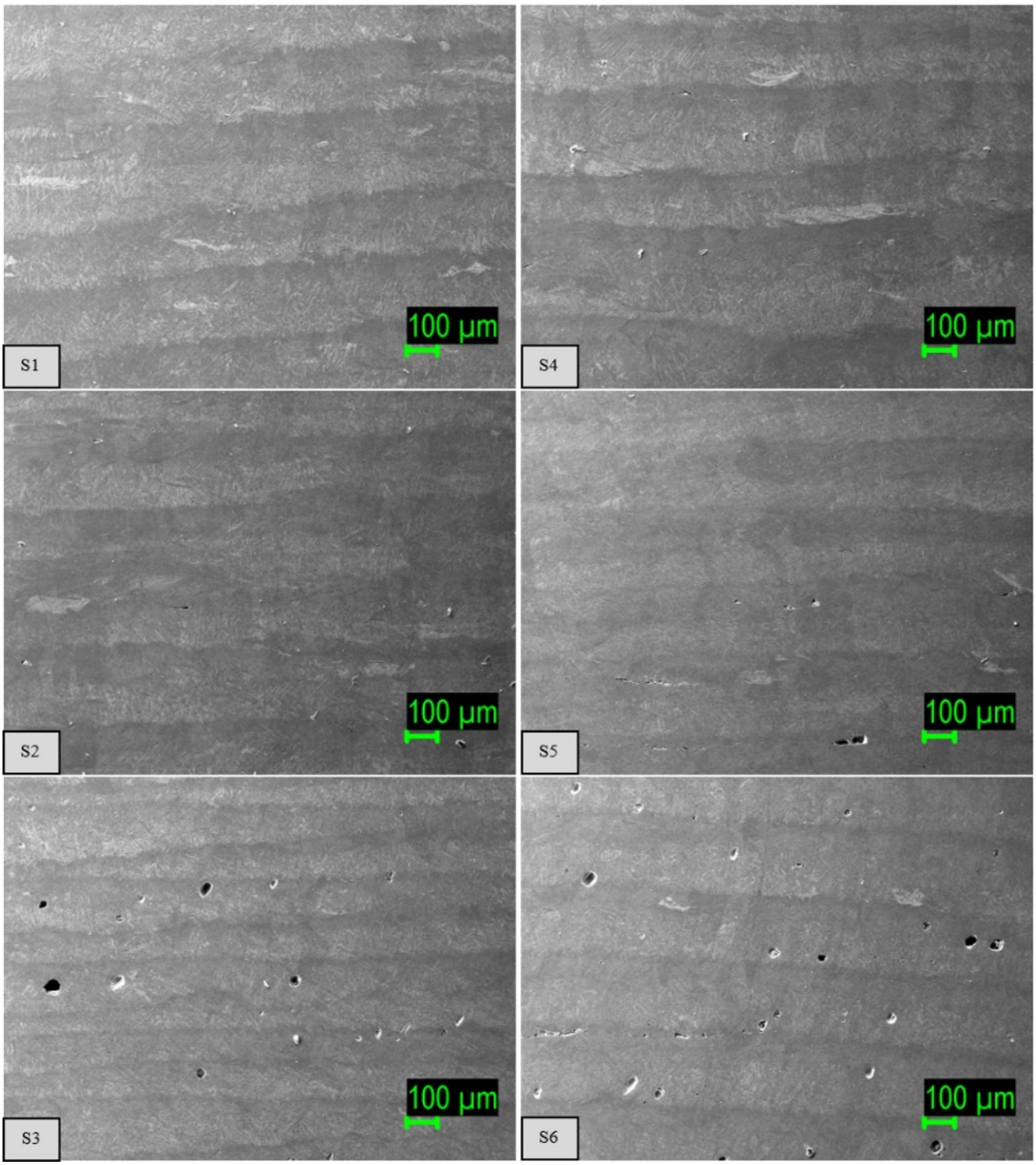


Fig. 10 SEM micrographs of the specimens illustrating surface morphology and pore characteristics

with lower porosity, corresponding to their lower VED values. As expected, minor absolute differences between µ-CT and Archimedes measurements were observed due to methodological factors; however, both methods showed the same porosity severity trends in all specimens.

Pore-size statistics were quantified directly from the segmented µ-CT datasets using the Feret diameter analysis tools implemented in Dragonfly. For all six specimens, the minimum, maximum, and mean Feret diameters were extracted from the complete set of segmented pores, and

the resulting quantitative values are summarized in Table 5, offering a representative statistical description of the pore-size distribution.

3.6 Numerical analysis of the developed porosity prediction model

The predictive fidelity of the finite volume-based thermal simulation algorithm was evaluated through comparative analysis with experimentally measured porosity trends. All numerical simulations were performed using a fixed spatial resolution of 1 μm voxel size and a constant temporal discretization, thereby ensuring consistent numerical conditions across all cases (Fig. 13). Consequently, variations in predicted porosity levels are attributable solely to differences in process parameters, including laser power, scan speed, and scanning strategy.

As illustrated in Fig. 14, the analysis focused on evaluating the model's capability to reproduce the relative distribution and severity of porosity across the six fabricated Ti6Al4V specimens. Emphasis was placed on the level of agreement between numerical predictions and experimental measurements, thereby reinforcing the model's effectiveness in capturing the thermally driven mechanisms underlying defect formation in PBF-LB processes.

Figure 15 illustrates the thermal simulation outputs for the six fabricated Ti6Al4V specimens (S1–S6), which exhibit distinct temperature distributions governed by variations in process parameters, particularly laser power, scan speed, and scanning strategy. Although all simulations employed identical spatial and temporal discretization (voxel size: 1 μm), the algorithm produced markedly different thermal fields, underscoring its sensitivity to changes in energy input. The higher thermal intensities observed in specimens S3 and S6, fabricated under elevated energy densities, correlate with the increased porosity levels measured experimentally.

Figures 15 and 16 present the predicted porosity levels generated by the developed simulation algorithm for each of the six Ti6Al4V specimens. The results reveal a clear and consistent ranking that aligns well with experimental trends obtained from both Archimedes density measurements and μ-CT imaging. Specimens processed with higher volumetric energy densities, such as S3 and S6, display elevated porosity predictions, in agreement with experimentally observed increases in pore volume. Notably, the algorithm reproduces the relative severity and ordering of porosity across all specimens without the need for empirical calibration or data fitting, highlighting its predictive robustness and physical consistency. This agreement confirms the model's capacity to capture parameter-driven defect formation mechanisms in PBF-LB processes within a first-principles thermal framework.

Although insufficiently melted regions are inherently included in the predicted unmelted volume, the present model reports porosity as a single volumetric metric without distinguishing between specific pore formation mechanisms such as lack-of-fusion, keyhole, or gas-entrapped pores.

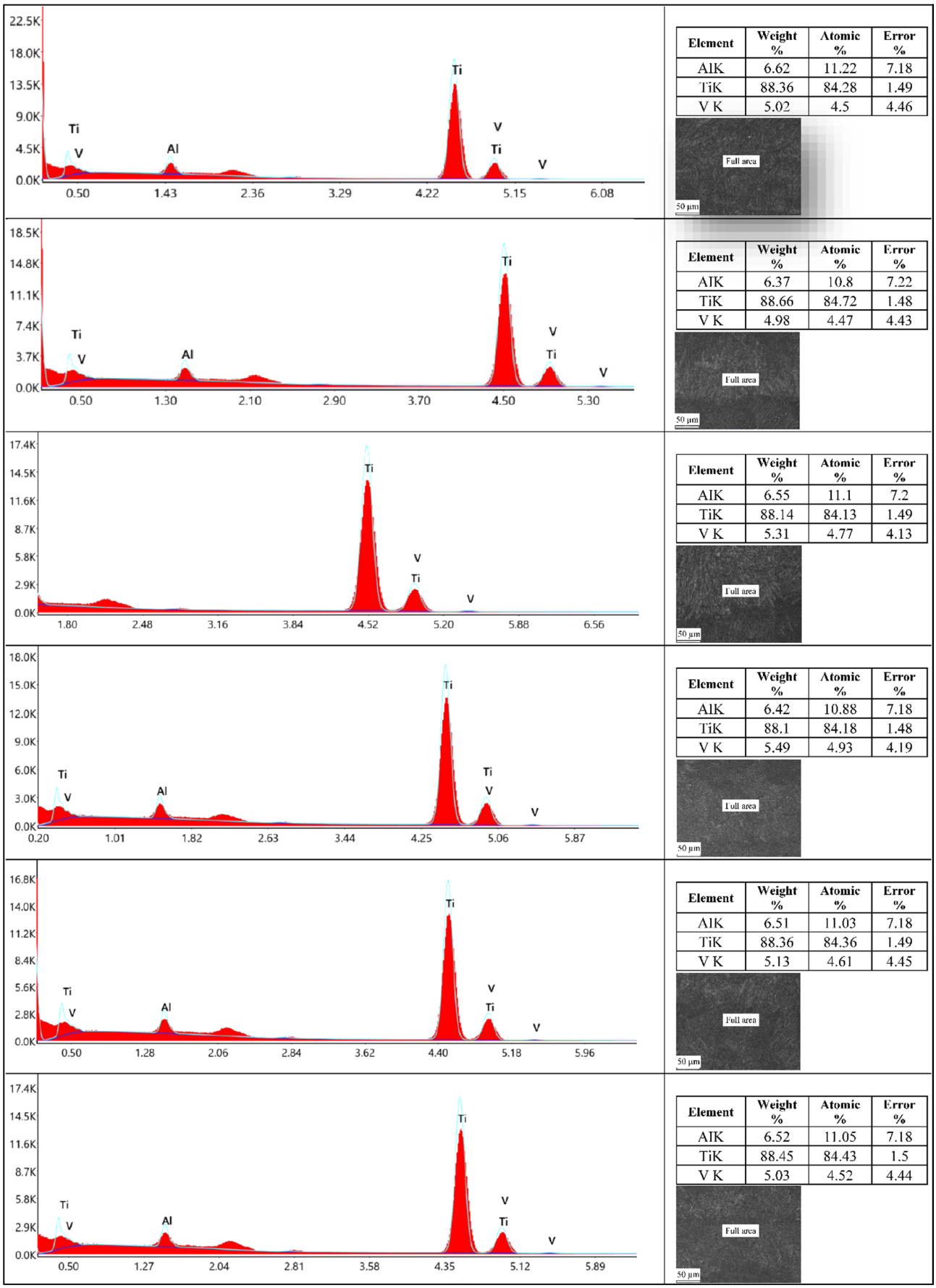
While the predicted porosity magnitudes correspond closely to experimental values, detailed spatial comparison with μ-CT segmentation results reveals discrepancies in pore localization. In particular, the algorithm's voxel-wise thermal analysis does not yet capture certain stochastic effects or geometric artifacts that influence the precise spatial distribution of pores within the build. These differences highlight the need for further refinement of the thermal-to-porosity mapping strategy, potentially through the incorporation of layer-wise temporal effects, powder packing variability, or in-situ monitoring data. Addressing these limitations will be critical for advancing the algorithm toward full-field, spatially resolved porosity prediction suitable for integration into digital twin architectures and defect-aware process control systems.

4 Conclusions

This study presents the development and implementation of a physics-informed porosity prediction algorithm tailored for Ti6Al4V components fabricated by the PBF-LB process. Built upon a finite volume-based thermal simulation framework, the model computes voxel-wise transient temperature distributions with a fixed spatial resolution of 1 μm and constant time step, thereby ensuring high spatial and temporal fidelity. Unlike data-driven approaches or empirically tuned models, the algorithm relies exclusively on first-principles thermal behavior, incorporating temperature thresholds associated with melt instability to identify and quantify pore-prone regions across the build volume.

The predictive accuracy of the model was rigorously validated against experimental data obtained from Archimedes density measurements and μ-CT. The algorithm successfully reproduced the relative ordering and severity of porosity across six specimens fabricated under distinct process parameter sets, without requiring parameter-specific calibration or additional experimental input beyond the initial processing conditions. This alignment demonstrates the model's capability to capture the thermodynamically driven nature of defect formation and its sensitivity to process variations such as laser power, scan speed, and scan strategy.

Despite these strengths, the model shows limitations in spatial accuracy when predicting the precise localization of pores. Although predicted porosity levels align quantitatively with experimental findings, discrepancies were observed in the spatial distribution of pores, particularly when compared



Element	Weight %	Atomic %	Error %
AlK	6.62	11.22	7.18
TiK	88.36	84.28	1.49
V K	5.02	4.5	4.46

Element	Weight %	Atomic %	Error %
AlK	6.37	10.8	7.22
TiK	88.66	84.72	1.48
V K	4.98	4.47	4.43

Element	Weight %	Atomic %	Error %
AlK	6.55	11.1	7.2
TiK	88.14	84.13	1.49
V K	5.31	4.77	4.13

Element	Weight %	Atomic %	Error %
AlK	6.42	10.88	7.18
TiK	88.1	84.18	1.48
V K	5.49	4.93	4.19

Element	Weight %	Atomic %	Error %
AlK	6.51	11.03	7.18
TiK	88.36	84.36	1.49
V K	5.13	4.61	4.45

Element	Weight %	Atomic %	Error %
AlK	6.52	11.05	7.18
TiK	88.45	84.43	1.5
V K	5.03	4.52	4.44

Fig. 11 EDS spectra and corresponding elemental composition tables for specimens S1 to S6

with μ-CT reconstructions. An additional source of deviation arises from differences in temporal sequencing between the experimental and simulated conditions. In actual fabrication, all six specimens were produced simultaneously on the same build plate, introducing natural delays between successive layer depositions due to scanning sequence and hatch spacing. This inter-part thermal interaction leads to cumulative heat retention and layer-wise thermal coupling across

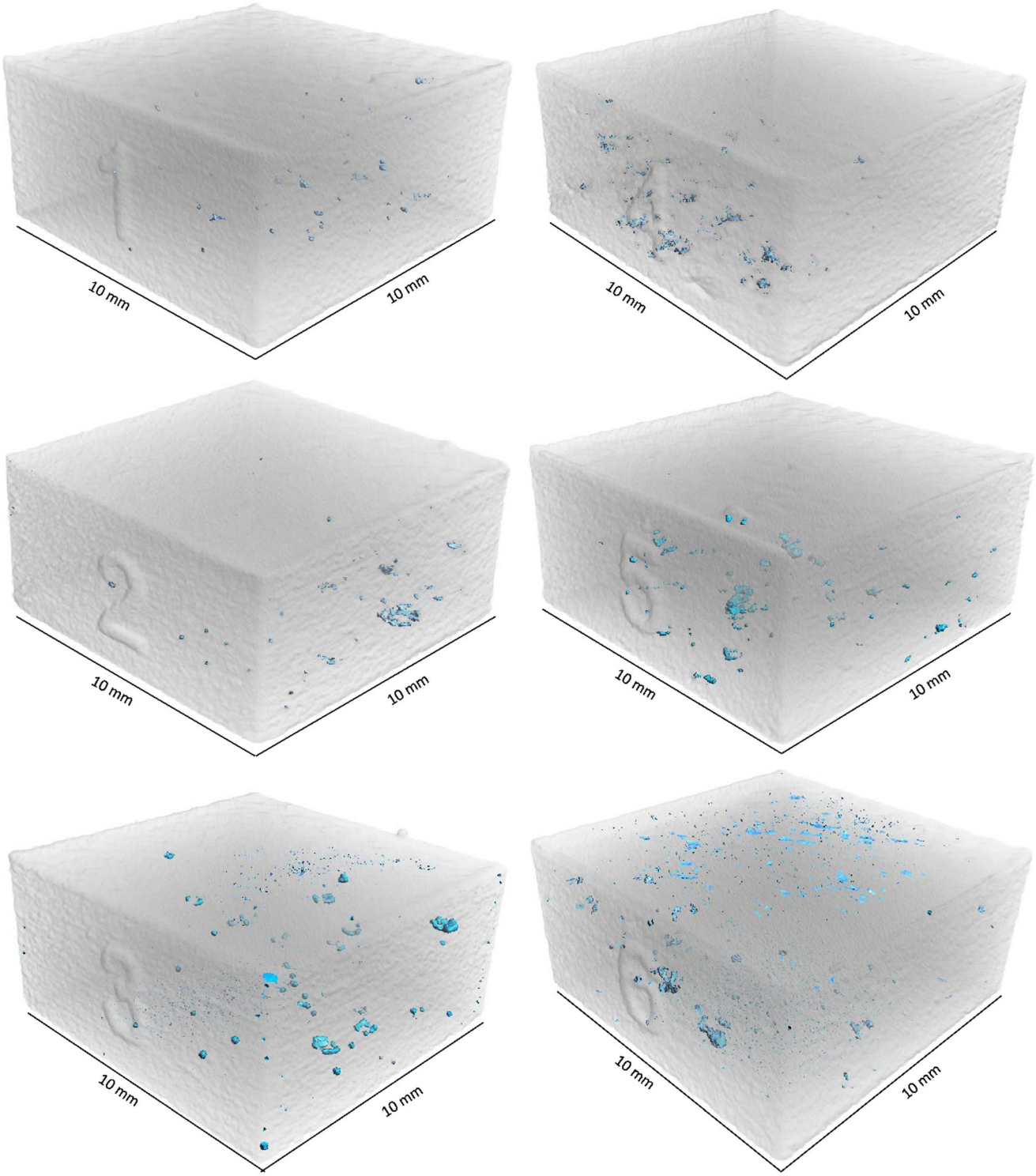


Fig. 12 3D porosity segmentation of six Ti6Al4V specimens obtained from μ-CT imaging. (Visualized with Dragonfly)

Table 5 Pore size statistics extracted from μ-CT segmentations

Sample No	Min diameter (mm)	Mean diameter (mm)	Max diameter (mm)
1	0.035	0.184	0.270
2	0.089	0.221	0.343
3	0.056	0.245	0.386
4	0.038	0.191	0.316
5	0.098	0.223	0.347
6	0.045	0.257	0.360

specimens. By contrast, the simulation models each part independently, assuming uniform interlayer time intervals and neglecting cross-part heat accumulation. As a result, the transient thermal histories in the model do not fully capture the complex interdependencies present in real builds, which may contribute to variations in predicted porosity magnitudes. Addressing this limitation will require either synchronized multi-part simulations or the integration of real build sequencing data into the thermal solver.

Future extensions of the algorithm will therefore focus on incorporating these additional physical and temporal effects, potentially through multi-physics coupling, synchronized multi-part simulations, and real-time data assimilation from in-situ monitoring systems. Such advancements will be critical for enabling spatially resolved, high-fidelity porosity predictions in practical additive manufacturing environments.

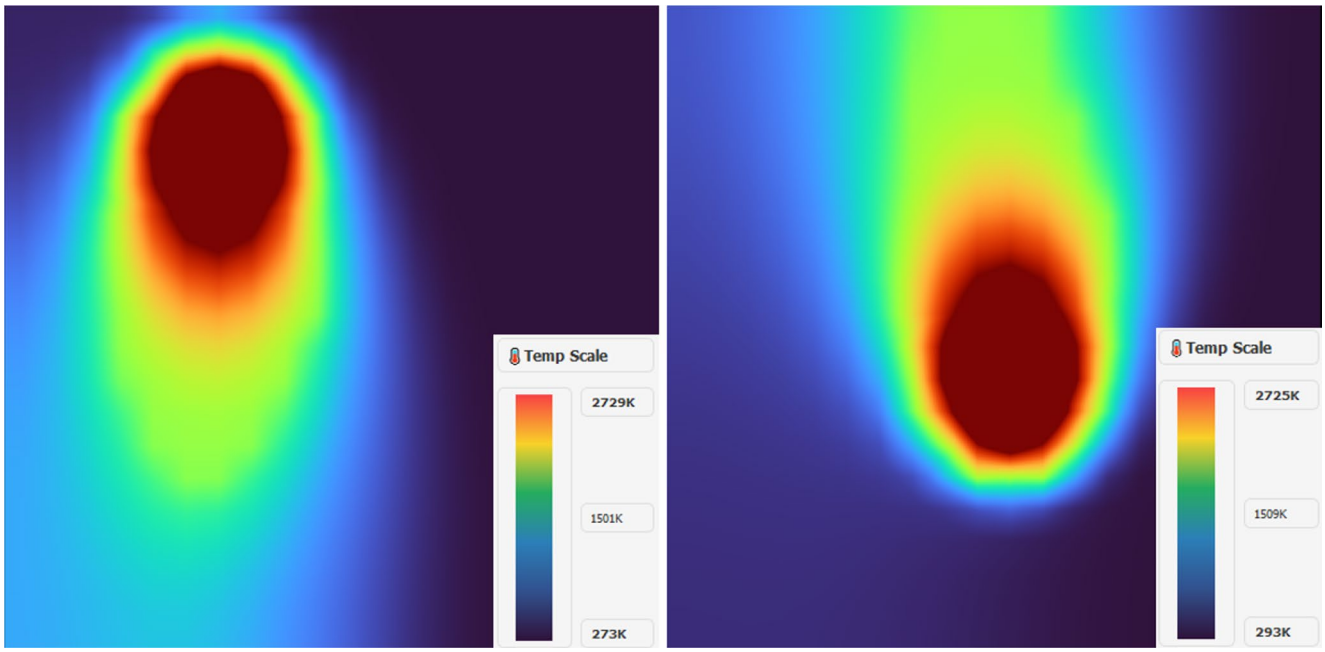


Fig. 13 Thermal simulation snapshots captured during scanning, showing two different moments of the same scan

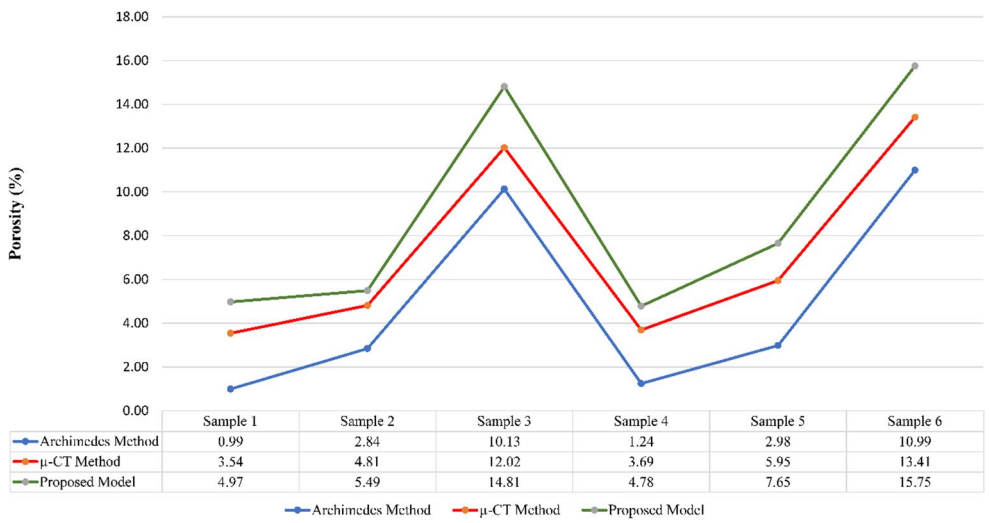


Fig. 14 Comparison of porosity results obtained via Archimedes method, μ-CT method, and the proposed model

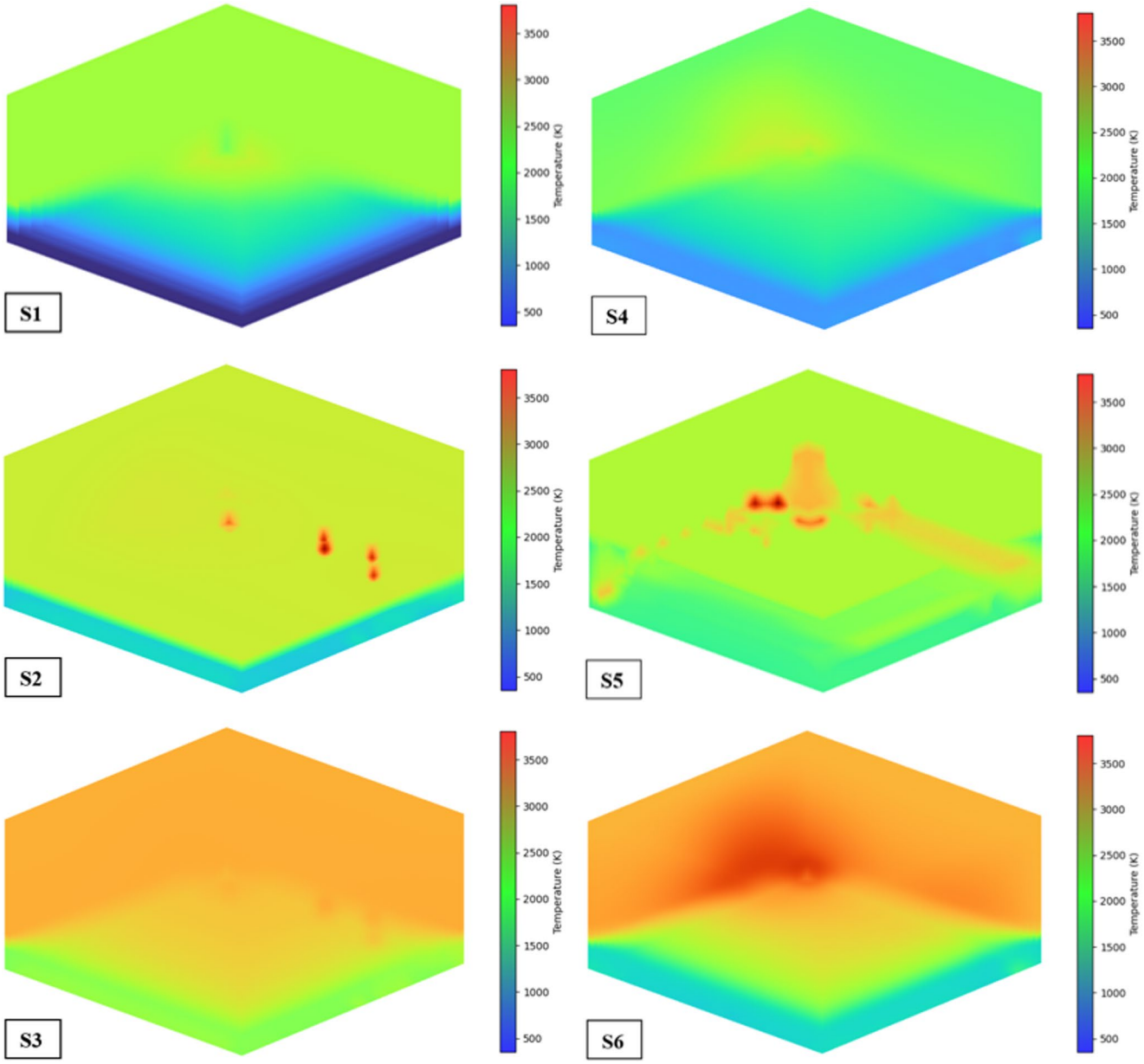


Fig. 15 Thermal simulation results for all specimens at a representative time step. The temperature distributions illustrate the influence of varying process parameters on localized heat accumulation and thermal gradients

Key findings of this study can be summarized as follows:

- A first-principles thermal model was developed using a finite volume framework with 1 µm spatial resolution and constant time step, requiring no empirical calibration.
- The algorithm accurately predicted relative porosity levels across six specimens produced with varying process parameters, in agreement with both Archimedes and µ-CT measurements.
- The model demonstrated strong sensitivity to laser power, scan speed, and scan strategy, effectively capturing their influence on thermal history and defect evolution.
- Spatial discrepancies in pore localization were observed, primarily due to the exclusion of stochastic physical phenomena such as melt pool dynamics, and spatter formation.

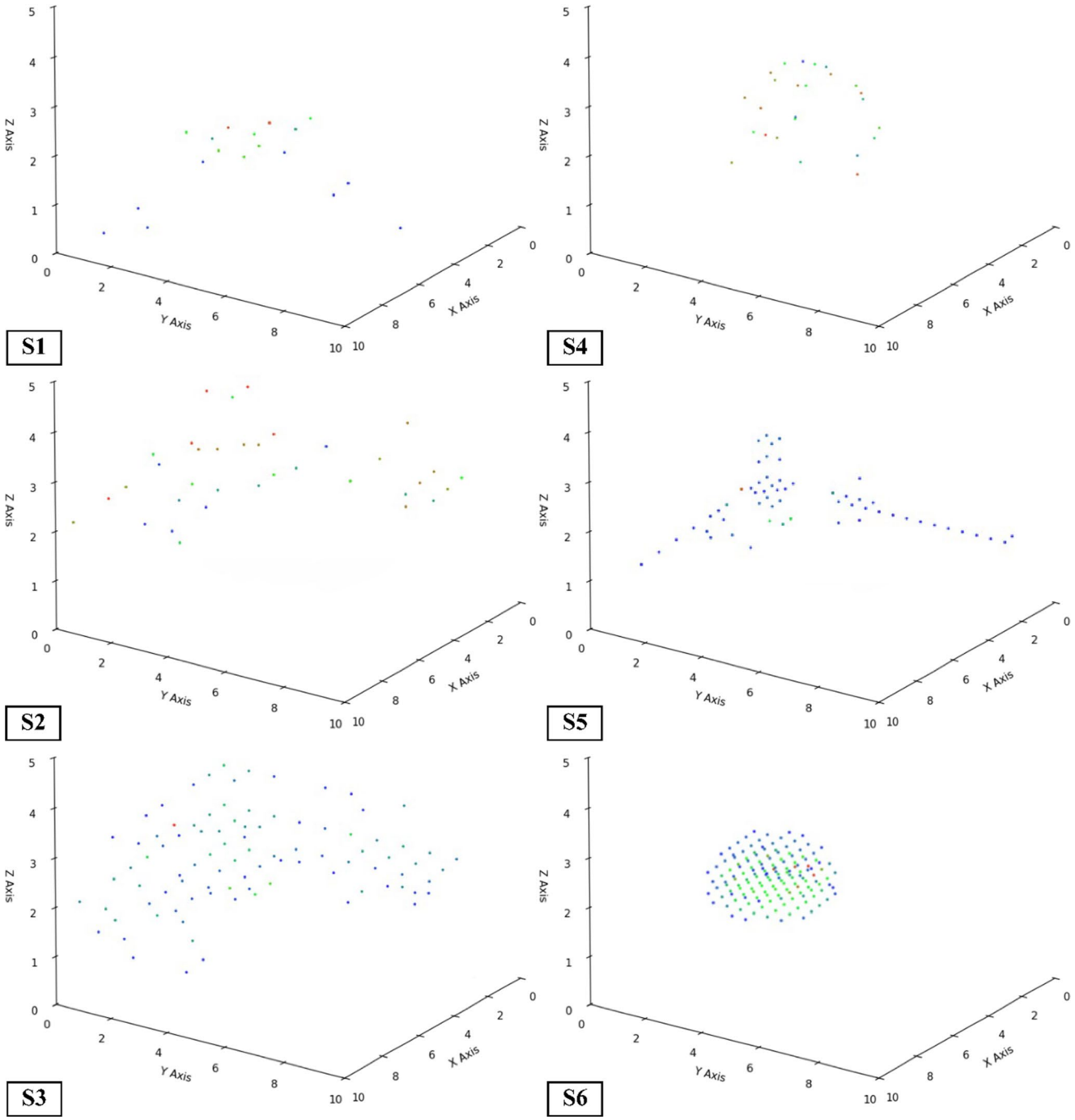


Fig. 16 Predicted porosity levels using the developed simulation algorithm for Ti6Al4V specimens fabricated by PBF-LB (axes in mm)

Acknowledgements The authors give a special thanks to Additive Manufacturing Technology Application and Research Center (EKTAM) for providing the necessary infrastructure for μ-CT analysis.

Author contributions Ibrahim Ulke: Conceptualization, formal analysis, investigation, methodology, resources, software, writing, original draft, and visualization. Oguzhan Yilmaz: Methodology and supervision. Mehmet Mollamahmutoglu: Supervision, validation, writing, review & editing, and software.

Funding Open access funding provided by the Scientific and Technological Research Council of Türkiye (TÜBİTAK). This study was supported by the Scientific and Technological Research Council of Türkiye (TÜBİTAK) under the 1002-A Short term Support Module (Project No: 22M575) and by the TÜBİTAK Directorate of Science Fellowships and Grant Programmes (BİDEB) through the 2211–A National PhD Scholarship Program. The authors also thank the Gazi University Academic Writing Center for proofreading support.

Data availability All data generated or analyzed during this study are included in this published article.

Declarations

Competing interests The authors declare that they have no known competing financial interests or personal relationships that could have appeared to influence the work reported in this paper.

Open Access This article is licensed under a Creative Commons Attribution 4.0 International License, which permits use, sharing, adaptation, distribution and reproduction in any medium or format, as long as you give appropriate credit to the original author(s) and the source, provide a link to the Creative Commons licence, and indicate if changes were made. The images or other third party material in this article are included in the article's Creative Commons licence, unless indicated otherwise in a credit line to the material. If material is not included in the article's Creative Commons licence and your intended use is not permitted by statutory regulation or exceeds the permitted use, you will need to obtain permission directly from the copyright holder. To view a copy of this licence, visit http://creativecommons.org/licenses/by/4.0/.

References

1. Zhou L et al (2024) Additive manufacturing: a comprehensive review. Sensors 24(9):2668. https://doi.org/10.3390/s24092668
2. Nyamekye P et al (2024) Sustainability aspects of additive manufacturing: leveraging resource efficiency via product design optimization and laser powder bed fusion. Heliyon 10(1):e23152. https://doi.org/10.1016/j.heliyon.2023.e23152
3. Jasik K, Śnieżek L, Kluczyński J (2025) Additive manufacturing of metals using the MEX method: process characteristics and performance Properties—A review. Materials 18(12):2744.https://doi.org/10.3390/ma18122744
4. Kladovasilakis N et al (2021) Impact of metal additive manufacturing parameters on the powder bed fusion and direct energydeposition processes: A comprehensive review. Progress Additive Manuf 6:349–365. https://doi.org/10.1007/s40964-021-00180-8
5. Smith C et al (2025) Assessing volumetric energy density as a predictor of defects in laser powder bed fusion 316L stainless steel. Jom 77(2):737–748
6. Reijonen J et al (2024) Effect of laser focal point position on porosity and melt pool geometry in laser powder bed fusion additive manufacturing. Additive Manuf 85:104180
7. Dar J et al (2025) A review on scan strategies in laser-based metal additive manufacturing. J Mater Res Technol 36:5425–5467
8. Snow Z, Nassar AR, Reutzel EW (2020) Invited Review Article: Review of the formation and impact of flaws in powder bed fusion additive manufacturing. Additive Manuf 36:101457
9. Guo L et al (2023) Identifying the keyhole stability and pore formation mechanisms in laser powder bed fusion additive manufacturing. J Mater Process Technol 321:118153
10. Huang Y et al (2022) Keyhole fluctuation and pore formation mechanisms during laser powder bed fusion additive manufacturing. Nat Commun 13(1):1170
11. Miner JP et al (2024) Impact of melt pool geometry variability on lack-of-fusion porosity and fatigue life in powder bed fusion-laser beam Ti–6Al–4V. Additive Manuf 95:104506
12. Nasrabadi HB et al (2025) XCT-assisted micromechanical modeling of the effect of pores on the plastic deformation and mechanical characteristics of PBF-LB/M-produced copper alloys. Mater Sci Engineering: A 924:147836
13. Kan WH et al (2022) A critical review on the effects of process-induced porosity on the mechanical properties of alloys fabricated by laser powder bed fusion. J Mater Sci 57(21):9818–9865
14. Rao J et al (2023) Non-destructive testing of metal-based additively manufactured parts and processes: a review. Virtual Phys Prototyp 18(1):e2266658
15. Ashebir DA et al (2024) Detecting multi-scale defects in material extrusion additive manufacturing of fiber-reinforced thermoplastic composites: a review of challenges and advanced non-destructive testing techniques. Polymers 16(21):2986
16. Staszewska A et al (2024) A machine learning methodology for porosity classification and process map prediction in laser powder bed fusion. Progress Additive Manuf 9(6):1901–1911
17. Atwya M, Panoutsos G (2024) -situ porosity prediction in metal powder bed fusion additive manufacturing using spectral emissions: a prior-guided machine learning approach. J Intell Manuf 35(6):2719–2742
18. Shafiei A et al (2022) Artificial neural network, support vector machine, decision tree, random forest, and committee machine intelligent system help to improve performance prediction of low salinity water injection in carbonate oil reservoirs. J Petrol Sci Eng 219:111046
19. Pi Q et al (2024) Predicting the porosity of as-built additive manufactured samples based on machine learning method for small datasets. Opt Laser Technol 177:111203
20. Mohamed AMF et al (2025) A novel porosity prediction framework based on reinforcement learning for process parameter optimization in additive manufacturing. Scripta Mater 255:116377
21. Oster S et al (2024) A deep learning framework for defect prediction based on thermographic in-situ monitoring in laser powder bed fusion. J Intell Manuf 35(4):1687–1706
22. Inayathullah S, Buddala R (2024) Review of machine learning applications in additive manufacturing. Results Eng 103676
23. Barrionuevo GO et al (2021) Comparative evaluation of supervised machine learning algorithms in the prediction of the relative density of 316L stainless steel fabricated by selective laser melting. Int J Adv Manuf Technol 113:419–433
24. Bhandarkar VV, Das B, Tandon P (2025) Real-time remote monitoring and defect detection in smart additive manufacturing for reduced material wastage. Measurement 252:117362
25. Tian Q et al (2021) Deep learning-based data fusion method for in situ porosity detection in laser-based additive manufacturing. J Manuf Sci Eng 143(4):041011

26. Wang S et al (2022) Nondestructive investigation on close and open porosity of additively manufactured parts using an X-ray computed tomography. Mater Today: Proc 70:124–130
27. Liu W et al (2020) Study of pore defect and mechanical properties in selective laser melted Ti6Al4V alloy based on X-ray computed tomography. Mater Sci Engineering: A 797:139981
28. Xi H et al (2024) Laser ultrasonic inspection of internal porosity defects in AlSi10Mg additive manufacturing components. Int J Lightweight Mater Manuf 7(4):546–555
29. Lin Y et al (2024) Porosity evaluation and analysis for 316L stainless steel by selective laser melting using laser ultrasonic technology. Int J Precis Eng Manuf 25(6):1209–1218
30. D'Accardi E et al (2024) Online monitoring of direct laser metal deposition process by means of infrared thermography. Progress Additive Manuf 9(4):983–1001
31. Dwivedi A, Khurana MK, Bala YG (2025) A comparative study of porosity rate measurement methods and influence of energy density in Inconel 718 produced by laser powder bed fusion additive manufacturing process. Int J Interact Des Manuf 19:2645–2658. https://doi.org/10.1007/s12008-024-01875-2
32. Peng X et al (2023) A review of in situ defect detection and monitoring technologies in selective laser melting. 3D Print Addit Manuf 10(3):438–466
33. Chen K et al (2024) A review of machine learning in additive manufacturing: design and process. Int J Adv Manuf Technol 135(3):1051–1087
34. Moradi A et al (2025) Intelligent laser-based metal additive manufacturing: A review on machine learning for process optimization and property prediction. Int J Adv Manuf Technol 136(2):527–560
35. Liu H et al (2024) Inference of highly time-resolved melt pool visual characteristics and spatially-dependent lack-of-fusion defects in laser powder bed fusion using acoustic and thermal emission data. Additive Manuf 83:104057
36. Guo S et al (2022) Machine learning for metal additive manufacturing: towards a physics-informed data-driven paradigm. J Manuf Syst 62:145–163
37. Farrag A et al (2025) Physics-informed machine learning for metal additive manufacturing. Progress Additive Manuf 10(1):171–185
38. Schreter-Fleischhacker M et al (2025) A consistent diffuse-interface finite element approach to rapid melt–vapor dynamics in metal additive manufacturing. arXiv preprint arXiv:2501.18781
39. Slama MB, Chatti S, Kolsi L (2023) Effect of processing parameters on porosity defects during SLM: a DOE-FEM approach. Weld World 67(9):2201–2213
40. Sarkar D, Kapil A, Sharma A (2024) *Advances in computational modeling for laser powder bed fusion additive manufacturing: a comprehensive review of finite element techniques and strategies.*. Addit Manuf. https://doi.org/10.1016/j.addma.2024.104157
41. Lee K-H, Yun GJ (2020) A novel heat source model for analysis of melt pool evolution in selective laser melting process. Additive Manuf 36:101497
42. Moraru E et al (2018) Some technological particularities on the execution of dental prostheses realized by selective laser deposition. J Optoelectron Adv Mater 20(3–4):208–213
43. Eliasu A, Czekanski A, Boakye-Yiadom S (2021) Effect of laser powder bed fusion parameters on the microstructural evolution and hardness of 316L stainless steel. Int J Adv Manuf Technol 113:2651–2669
44. Buhairi MA et al (2023) Review on volumetric energy density: influence on morphology and mechanical properties of Ti6Al4V manufactured via laser powder bed fusion. Progress Additive Manuf 8(2):265–283
45. Wang J et al (2023) Understanding melt pool characteristics in laser powder bed fusion: an overview of single-and multi-track melt pools for process optimization. Adv Powder Mater 2(4):100137
46. Yildiz AK, Mollamahmutoglu M, Yilmaz O (2022) Computational evaluation of temperature-dependent microstructural transformations of Ti6Al4V for laser powder bed fusion process. J Mater Eng Perform 31(9):7191–7203
47. Bartsch K et al (2021) Material modeling of Ti–6Al–4V alloy processed by laser powder bed fusion for application in macro-scale process simulation. Mater Sci Engineering: A 814:141237
48. Mollamahmutoglu M et al (2022) The effect of evaporation and recoil pressure on energy loss and melt pool profile in selective electron beam melting. Int J Adv Manuf Technol 120(5):4041–4050
49. Dutta J, Bhanja D, Narendranath S (2023) Theoretical evolution of thermal behaviour of Ti-6Al-4V subjected to selective laser melting: A powder free approach. Optik 273:170483
50. Mishra AK, Kumar A (2019) Numerical and experimental analysis of the effect of volumetric energy absorption in powder layer on thermal-fluidic transport in selective laser melting of Ti6Al4V. Opt Laser Technol 111:227–239
51. Yao B et al (2024) Process parameter optimization for selective laser melting Ti-6Al-4V with high layer thickness. Mater Today Commun 41:110781
52. Hacısalihoğlu I, Yıldiz F, Çelik A (2021) The effects of build orientation and hatch spacing on mechanical properties of medical Ti–6Al–4V alloy manufactured by selective laser melting. Mater Sci Engineering: A 802:140649
53. Ullah A et al (2025) Effects of laser beam shaping on Ti-6Al-4V single tracks in PBF-LB/M: a study with Aconity MIDI+. Opt Laser Technol 192:113762
54. Aichouch I, El Magri A, Hammouti B (2025) Influence of laser power and scan speed on porosity, microhardness, and corrosion resistance in HCl medium of additively manufactured H13 tool steel. Prog Addit Manuf. https://doi.org/10.1007/s40964-025-01068-7

Publisher's Note Springer Nature remains neutral with regard to jurisdictional claims in published maps and institutional affiliations.